

Prospects for observing the magnetorotational instability in the Plasma Couette Experiment

K. FLANAGAN¹†, M. CLARK, C. COLLINS, C. COOPER,
I. V. KHALZOV, J. WALLACE AND C. B. FOREST

¹Department of Physics, University of Wisconsin, Madison, WI 53706, USA

(Received ?; revised ?; accepted ?. - To be entered by editorial office)

Many astrophysical disks, such as protoplanetary disks, are in a regime where non-ideal, plasma-specific MHD effects can significantly influence the behavior of the magnetorotational instability (MRI). The possibility of studying these effects in the Plasma Couette Experiment (PCX) is discussed. An incompressible, dissipative global stability analysis is developed to include plasma-specific two-fluid effects and neutral collisions, which are inherently absent in analyses of Taylor-Couette flows in liquid metal experiments. It is shown that at current PCX parameters, the ion-neutral drag significantly affects the azimuthal velocity profile, thus limiting the flows to regime where the MRI is not present. Electrically driven flow (EDF) is proposed as an alternative in which the MRI can destabilize at more easily achievable plasma parameters. Scenarios for reaching MRI relevant parameter space and necessary hardware upgrades are described.

1. Introduction

The magnetorotational instability (MRI), first derived by Velikhov (1959) and Chandrasekhar (1960), has been studied extensively as a possible mechanism of enhanced angular momentum transport in accretion disks (Balbus & Hawley 1991, 1998). In an idealized form, this instability occurs when conducting fluid in a spinning disk is threaded by a weak magnetic field. In order to excite the instability the fluid must have an angular velocity profile which is decreasing with radius, $\partial\Omega^2/\partial\ln r < 0$, and the magnetic field must be sufficiently weak as to not stabilize perturbations, $(\mathbf{k} \cdot \mathbf{V}_A)^2 < -\partial\Omega^2/\partial\ln r$. In some plasmas, such as weakly-ionized and sparse protoplanetary disks, these ideal MHD conditions may not fully describe the onset of MRI, nor the dynamics in the fully saturated state of MRI-driven turbulence. For example, the two-fluid Hall effect can become important when ions become decoupled from the magnetic field. Consequently, MRI growth only occurs when the magnetic field is antiparallel to the rotation axis (Wardle 1999; Balbus & Terquem 2001). Recent work by Kunz & Lesur (2013); Lesur *et al.* (2014) suggests that two-fluid and neutral effects are necessary for qualitatively correct descriptions of the MRI in protoplanetary discs.

In nature, the ratio of viscosity and resistivity, a property described by the magnetic Prandtl number, $Pm = \mu_0\sigma\nu$, can vary by many orders of magnitude: $Pm \lesssim 10^{-5}$ in disks around young stellar objects while $Pm \gtrsim 10^5$ around active galactic nuclei. Shearing box simulations have shown that varying $Pm = 0.06 - 4$ can cause the magnitude of the MRI driven turbulent radial momentum transport to vary by two orders of magnitude (Longaretti & Lesur 2010), suggesting that the MRI may not be efficient at small

† Email address for correspondence: ksflanagan@wisc.edu

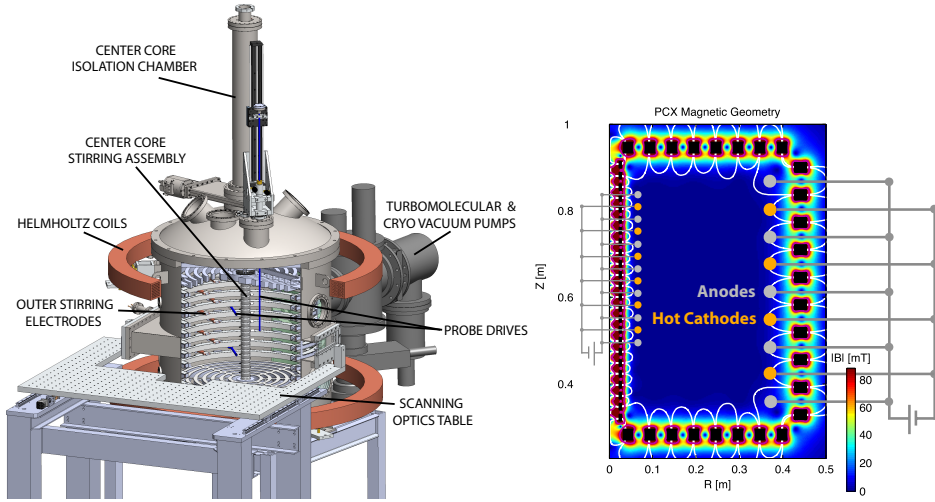


FIGURE 1. Left: A cutaway view of PCX showing the major subsystems. Right: The magnetic field geometry of PCX showing electrodes at both the inner and outer boundaries.

Prandtl numbers. Unfortunately for liquid metal experiments, Pm is fixed at $\sim 10^{-5}$, thus making them susceptible to Ekman circulation driven turbulence and very small saturated amplitudes (Gissinger *et al.* 2012). However, in plasmas $Pm \propto n^{-1}T_e^{3/2}T_i^{-5/2}$ and can be adjusted by varying the density and temperature. Because of the importance of two-fluid and neutral collision effects in real astrophysical systems and the adjustable Pm , plasma experiments are ideal for laboratory study of the MRI.

In the Plasma Couette Experiment (PCX), a hot, fast-flowing, steady-state plasma has recently been created and confined in a largely magnetic field-free volume. Differential rotation is driven via electrostatic stirring at inner and outer boundaries of a cylindrical plasma volume (Collins *et al.* 2012, 2014). Flows up to 12 km/s in helium are routinely created, corresponding to $Rm \sim 65$. To observe the MRI these flow profiles must be adjusted to mimic Keplerian-like flows of astrophysical accretion disks, where angular velocity is decreasing with radius while still maintaining Rayleigh hydrodynamic stability with angular momentum increasing with radius. In PCX, the range of achievable densities and temperatures set $Pm \approx 10^{-1} - 10^2$.

This article begins by examining the effects of resistive and viscous dissipation, the Hall term, and plasma-neutral interactions pertinent to the onset of MRI in PCX. First, a description of PCX as it currently exists is provided. The experiment has thus far operated with weakly-ionized ($\lesssim 1\%$) plasmas, where charge exchange collisions between ions and neutrals can have significant effects on the shape of flow profiles (Collins *et al.* 2012). Next, currently underway upgrades to PCX are described. These upgrades seek to improve the confinement, thus increasing both the plasma density and temperature in PCX. A global stability analysis of the MRI that includes neutral drag and two-fluid effects is then presented. This analysis is carried out with parameters that match those expected in the PCX upgrade. Finally, an alternative mechanism for driving flow with a body force across the whole plasma profile, which we simply call electrically driven flow (EDF), is described along with a preliminary MRI stability analysis for PCX parameters.

	PCX	PCX-U
n_e (cm ⁻³)	10 ¹⁰ – 10 ¹¹	10 ¹¹ – 10 ¹²
T_e (eV)	5 – 10	10 – 20
T_i (eV)	0.1 – 0.5	0.5 – 1
$f\%$	0.1 – 10%	1 – 99%
Pm	0.2 – 200	0.5 – 350
Rm	0 – 500	0 – 1600
Ha	40 – 80	30 – 50
M	0.5 – 0.7	0.3 – 0.5
$\mu \equiv R_1/L_\nu$	0.1 – 10	0.02 – 2
$\delta_i \equiv c/(\omega_{pi}R_1)$	5 – 50	2 – 15

TABLE 1. Plasma parameter and dimensionless variable ranges for both PCX and PCX-U. For the Hartmann number (Ha), a magnetic field of $B_0 = -2$ Gauss is used. The Mach number is based on velocity at the inner radius and ion sound speed: $M = V_1/C_s$. The unit of length used in this paper is the inner stirring radius $R_1 = 0.1$ m.

2. Description of Experiment

PCX consists of a roughly 1 m tall by 1 m diameter cylindrical vacuum chamber. The inner walls of the chamber are lined with toroidal rings of permanent magnets. This magnet geometry is shown in Fig 1. The rings alternate polarity creating a strong multi-cusp magnetic field isolated to the edge of the vessel. This field confines the plasma losses to a small cusp on the face of the magnets, while leaving the bulk volume unmagnetized. If desired, an external Helmholtz coil can produce nearly uniform axial magnetic fields in the chamber up to $B_0 \sim 50$ G.

A plasma discharge is created by biasing emissive thoriated tungsten cathodes to cold molybdenum anodes at up to 600V. The plasma is then heated with up to 6kW of electron cyclotron heating (ECH). Table 1 shows typical PCX plasma parameters along with the relevant dimensionless quantities for this paper.

The hot cathodes also act to stir the plasma by drawing a current across the multi-cusp magnetic field at the edge. This $\mathbf{J} \times \mathbf{B}$ torque viscously couples inward to the unmagnetized bulk plasma. Due to the axisymmetric configuration of the magnets, particle drifts in the magnetized edge act to symmetrize the system, such that the toroidal location of the cathodes and anodes does not affect the flow drive (Katz *et al.* 2012). Flow can be driven at the inner boundary by a center core assembly consisting of 22 stacked magnet rings and up to 8 smaller thoriated tungsten cathodes biased with respect to cold anodes. This assembly can be entirely removed via a gate valve for maintenance of the cathodes.

Plasmas in PCX are routinely diagnosed using a swept or triple tip Langmuir probe for electron temperature and density, a cold cathode gauge for neutral pressure, and Mach probes for flow velocity. In addition to these routine diagnostics, PCX has implemented Optical Emission Spectroscopy (OES) and a Fabry-Perot interferometer to measure electron and ion temperature, respectively. Both of these optical diagnostics are non-invasive, operating by simply sampling a single chord of emitted plasma light. The OES system takes a broadband spectrum of the plasma and uses line ratios to determine the electron temperature. OES temperature measurements in PCX agree within 15% of the routine Langmuir probe. The Fabry-Perot interferometer finely samples a small (< 1 nm) range of the emission spectrum centered at 468.6 nm in helium and 488 nm in argon. Ion emission lines at these wavelengths reflect the entire ion distribution function,

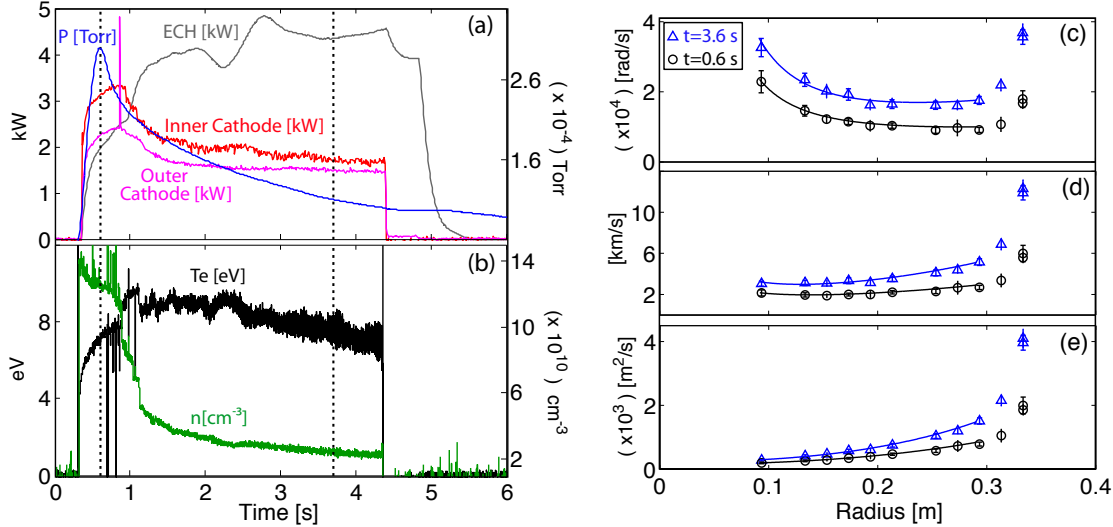


FIGURE 2. An example discharge from PCX. In (a) plasma is created with a neutral gas puff and ECH heating. The plasma is spun with four outer cathodes (each 350V, 1.1A) and five inner cathodes (each 575V, 0.75A). In (b) electron temperature and density as measured by the triple Langmuir probe. (c) The angular velocity profile is shown at two different times in the shot (shown as dashed vertical lines in (a) and (b)) along with the azimuthal velocity (d) and angular momentum (e) profiles. The error bars are standard deviation of fluctuation in time.

such that the ion temperature and velocity can be deduced. In initial measurements of non-flowing argon plasmas, the ion temperature was determined to be $T_i = 0.2 - 1$ eV.

2.1. Taylor-Couette Flow (TCF) Profiles with Ion-Neutral Drag

TCF profiles of up to 12.3 km/s on the outer boundary and 3.4 km/s on the inner have been driven in helium PCX plasmas (Collins *et al.* 2014). These flows, shown in Fig. 2, have areas of decreasing angular frequency as required by the ideal-MRI criteria. They also have increasing angular momentum, thus meet the Rayleigh criterion for hydrodynamic stability. At PCX plasma parameters, these flows correspond to a Reynolds number of $Re \approx 26$ (using the outer boundary velocity) and a magnetic Prandtl number of $Pm \approx 2.5$. However, these flows have thus far been obtained without applied axial magnetic field so no instabilities have yet been observed.

In weakly-ionized plasmas charge exchange collisions between neutrals and ions impose a drag force that affects the equilibrium (steady-state) velocity profiles (Collins *et al.* 2012). These profiles are a departure from ideal TCF yet still have a simple Bessel function form:

$$V_\phi(r) = A\mathcal{I}_1(r/L_\nu) + B\mathcal{K}_1(r/L_\nu) \quad (2.1)$$

where the constants A and B depend on the outer and inner boundary locations and the velocities applied, $L_\nu^2 \equiv \tau_{i0}\nu$ is the momentum diffusion length, $\tau_{i0} = (n_0 \langle \sigma_{cx} v \rangle)^{-1}$ is the ion-neutral collision time, σ_{cx} is the ion-neutral charge exchange cross section, and ν is the kinematic viscosity due to ion-ion collisions. The momentum diffusion length parametrizes the balance between the viscous momentum diffusion and the neutral drag. When $\mu \equiv R_1/L_\nu \gg 1$, the neutral drag dominates the viscous diffusion, rotation is confined to inner and outer edges of the plasma and the average velocity across the profile drops. In the opposite limit $\mu \ll 1$, the velocity profile becomes the ideal Taylor-

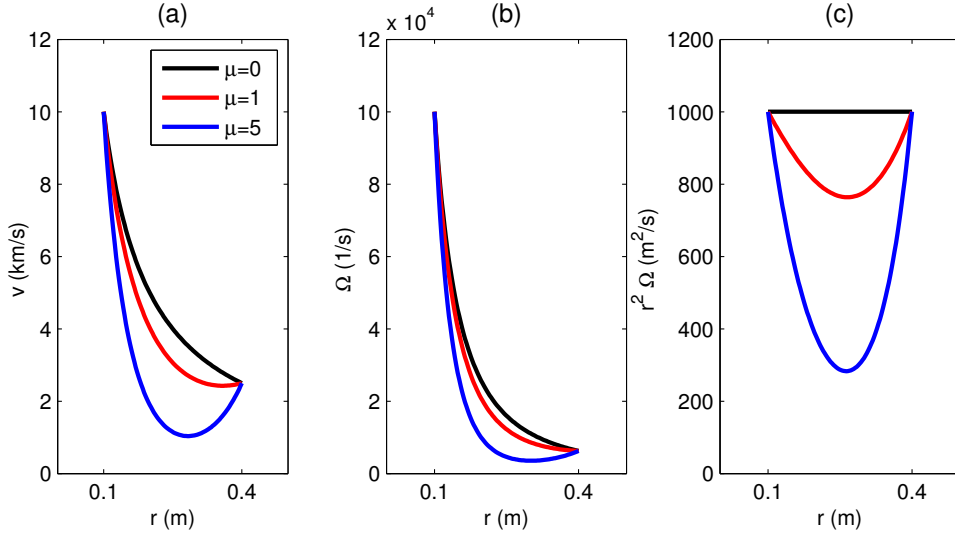


FIGURE 3. The (a) toroidal velocity, (b) angular frequency, and (c) angular momentum of modified Taylor Couette flow with different $\mu \equiv R_1/L_\nu$ values. The effect of the neutral drag is increased at greater values of μ .

Couette profile: $V_\phi(r) = ar + b/r$. Finite neutral drag has a large qualitative effect on the velocity profile and greatly affects the stability of this modified TCF. Fig. 3 highlights the effect of ion-neutral collisions on TCF profiles of toroidal velocity, angular frequency and angular momentum. The boundary velocities for these profiles are chosen to be $V_1 = 10$ km/s at $R_1 = 0.1$ m and $V_1 = 2.5$ km/s at $R_1 = 0.4$ m. With no neutrals this gives a toroidal velocity profile $V_\phi(r) \propto 1/r$, which is marginally stable to the Rayleigh criterion and meets the ideal MRI condition. Such a choice of boundary velocities also allows comparison of TCF with electrically driven flow, where $V_\phi(r) \propto 1/r$ is naturally realized in the bulk of the plasma (Section 5). The profiles shown in Fig. 3 have not been created on PCX due to the current limitations of the centerstack stirring assembly, but they are expected to be achieved in the upgraded experiment.

2.2. Proposed System Upgrades

An upgrade to the confinement and heating systems for PCX is underway. The goals are to improve confinement by increasing the volume to loss area ratio, \mathbb{V}/A_l , to input more power, and to improve the temperature tolerances of PCX in order to accommodate longer and higher power discharges. These upgrades, referred to as PCX-U from here on, constitute a major change for PCX that collectively aims to push the experiment into MRI relevant parameter regimes.

The largest portion of the PCX upgrade consists of an entirely new magnet assembly. Approximately 2000 samarium cobalt (SmCo) magnets, like those used in the Madison Plasma Dynamo Experiment (MPDX) (Cooper *et al.* 2014), will replace the current array of ceramic magnets. These relatively inexpensive magnets have a much higher field strength and temperature tolerance. For the sizes and grade proposed, the field will be approximately 4 kG at the face of the magnets (the ceramic magnets are 1 kG) and the maximum operating temperature will be nearly 300° C.

The new magnets themselves will be a significant improvement over the current system. Currently, the length of PCX discharges is mostly limited by the temperature that the magnets reach, which is ideally kept below about 60°C. With a higher temperature

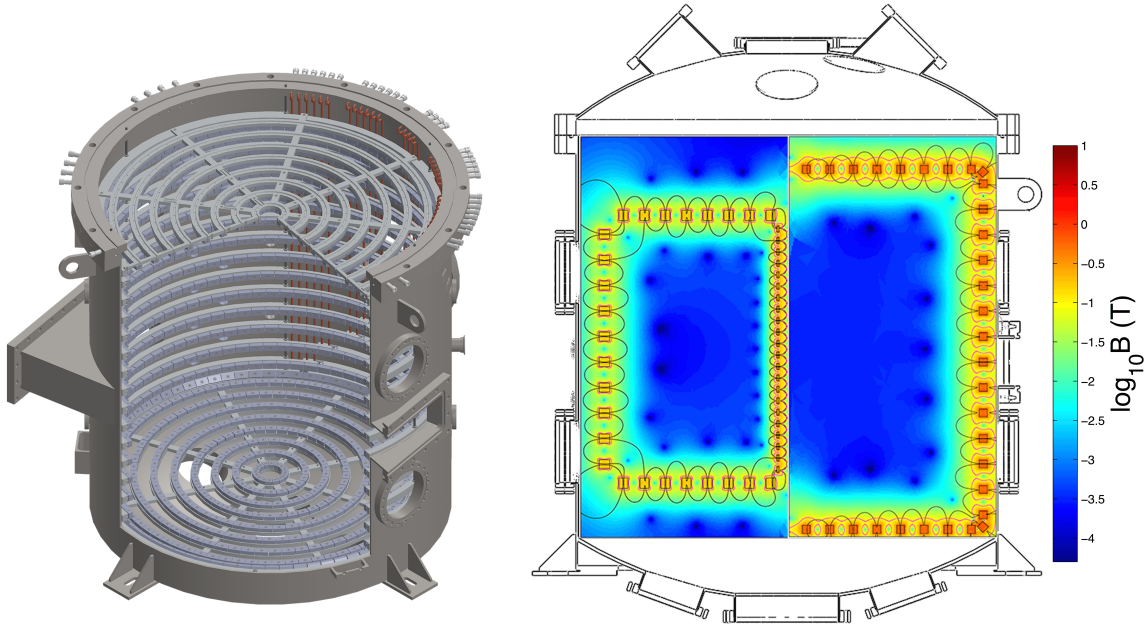


FIGURE 4. Left: A design image of the proposed new magnet assembly on PCX-U. Right: A comparison of the current PCX magnet geometry (left) and the proposed geometry (right). These plots show the magnitude of the magnetic field on a scale from Earth’s field to 1 T. The pink contour is the 875G ECRH resonance.

tolerance, the SmCo magnets will allow for longer discharges. In turn, good vacuum pumping and longer discharges will remove more neutrals. Additionally, the four-fold increase in magnetic field strength will reduce the cusp loss width. The cusp width can be estimated as $w = 4\sqrt{\rho_i\rho_e} \propto B^{-1}$, where ρ_i and ρ_e are the ion and electron gyroradii, respectively (Hershkovitz *et al.* 1975). This smaller width represents an increase in the ∇/A_l ratio.

The left image of Figure 4 shows a design image of the new magnet assembly. Approximately 1000 magnets are bolted to 14 individually water cooled aluminum rings equally spaced in the axial direction. At the top and bottom of the chamber, 8 concentric rings attached by spokes carrying water cooling support an additional 350 magnets each. Finally, two rings pitched at 45° are supported in the corners between the top and bottom rings and the side rings. These angled rings serve to strengthen the field at the corners where the current assembly suffers from the most magnet heating. The whole assembly is supported by 6 rods attached to a top flange which doubles as the water cooling vacuum feedthrough. The inner three rings on the top and bottom assemblies may be removed in order to place future centerstack assemblies of up to 16in in diameter into PCX-U.

On the right in Figure 4, a side by side comparison of the current and new magnet assemblies highlights the roughly 150% increase in plasma volume. Due to the extra rings of magnets, the cusp length of the new assembly is roughly 130% longer, but the stronger magnets make the cusp width smaller, so the ∇/A_l ratio is about 4.5 times larger on PCX-U. This is a significant improvement in confinement, which will allow higher plasma densities and temperatures.

In addition to the new magnet assembly, PCX-U includes a second 6kW magnetron for increased plasma heating, doubling the available microwave power to 12kW. At densities above, $n = 7.4 \times 10^{10} \text{ cm}^{-3}$, PCX plasmas are above the O-mode cutoff for 2.45 GHz,

yet it has been observed that microwave power still heats the plasma possibly via surface wave discharges (Collins *et al.* 2014). PCX-U is estimated to operate in this overdense mode. Additionally, the stronger field on the magnets will place the 875 G ECH resonance further into the plasma volume, thus the surface wave discharge will have a larger volume to fill. This extra power will be managed by the high temperature tolerance of the SmCo magnets.

3. Model for Global Stability Analysis

With the new upgrades coming online, a prediction of the onset conditions for MRI in PCX-U is called for. For this paper, we have implemented a global linear stability analysis. In order to capture Hall and neutral collision effects an incompressible dissipative Hall MHD model with neutral-ion collisions is used. The only two-fluid effect included is the Hall term. Ambipolar diffusion is negligible in PCX since recently charge-exchanged neutrals have a mean free path much longer than the machine size and thus are not coupled to the ions. The incompressibility assumption is justified by the relatively small values of Mach number (Table 1). The governing equations used for this analysis are:

$$\frac{\partial \mathbf{V}}{\partial t} = -(\mathbf{V} \cdot \nabla) \mathbf{V} - \nabla \frac{P}{\rho} + \frac{1}{\mu_0 \rho} (\nabla \times \mathbf{B}) \times \mathbf{B} + \nu \nabla^2 \mathbf{V} - \frac{1}{\tau_{i0}} \mathbf{V} \quad (3.1)$$

$$\nabla \cdot \mathbf{V} = 0 \quad (3.2)$$

$$\frac{\partial \mathbf{B}}{\partial t} = \nabla \times \left[\mathbf{V} \times \mathbf{B} - \frac{1}{\mu_0 n e} (\nabla \times \mathbf{B}) \times \mathbf{B} \right] + \eta \nabla^2 \mathbf{B} \quad (3.3)$$

$$\nabla \cdot \mathbf{B} = 0 \quad (3.4)$$

where P is the scalar pressure, ρ is the mass density and η is the magnetic diffusivity (in m^2/s). In these equations, plasma parameters n_e , ρ , τ_{i0} , ν and η are assumed to be constant and uniform throughout the volume. Profiles of T_e and n_e from Langmuir probes and the OES system support this assumption (Collins *et al.* 2014). The equilibrium modified TCF profile (2.1) results from the steady-state balance between the last two terms in (3.1). In order to study linear stability these equations are cast in terms of non-dimensional parameters and linearized near the equilibrium state: $\mathbf{V}_{eq} = V_\phi(r) \mathbf{e}_\phi$ and $\mathbf{B}_{eq} = B_0 \mathbf{e}_z$. The unit of length is the radius of the inner cylindrical boundary R_1 and the unit of velocity is the plasma velocity at this boundary, so $\mathbf{V} = V_1 \mathbf{v}$ and $P = \rho V_1^2 p$. The magnetic field is normalized by the applied axial field: $\mathbf{B} = B_0 \mathbf{b}$. The dimensionless equations are

$$\gamma \mathbf{v} = -(\mathbf{v}_{eq} \cdot \nabla) \mathbf{v} - (\mathbf{v} \cdot \nabla) \mathbf{v}_{eq} - \nabla p + \frac{1}{M_A^2} (\nabla \times \mathbf{b}) \times \mathbf{b}_{eq} + \frac{1}{Re} (\nabla^2 - \mu^2) \mathbf{v} \quad (3.5)$$

$$\gamma \mathbf{b} = \nabla \times \left[\mathbf{v}_{eq} \times \mathbf{b} + \mathbf{v} \times \mathbf{b}_{eq} - \frac{\delta_i}{M_A} (\nabla \times \mathbf{b}) \times \mathbf{b}_{eq} \right] + \frac{1}{Rm} \nabla^2 \mathbf{b} \quad (3.6)$$

where γ is the growth rate in units of angular frequency $\Omega_1 \equiv V_1/R_1$. The dimensionless parameters that enter these equations are: the fluid Reynolds number, $Re \equiv V_1 R_1 / \nu$; the magnetic Reynolds number, $Rm \equiv V_1 R_1 / \eta$; the Alfvén Mach number, $M_A \equiv V_1 / V_A \equiv V_1 \sqrt{\mu_0 \rho} / B_0$; the normalized ion inertial length for the Hall effect, $\delta_i \equiv d_i / R_1 \equiv c / (\omega_{pi} R_1)$; and the normalized momentum diffusion length for the neutral collision effect, $\mu \equiv R_1 / L_\nu \equiv (R_2 - R_1) / \sqrt{\tau_{i0} \nu}$.

Note that in this stability analysis the effect of the neutral drag enters consistently both through the modification of the equilibrium rotation profile and as a drag force

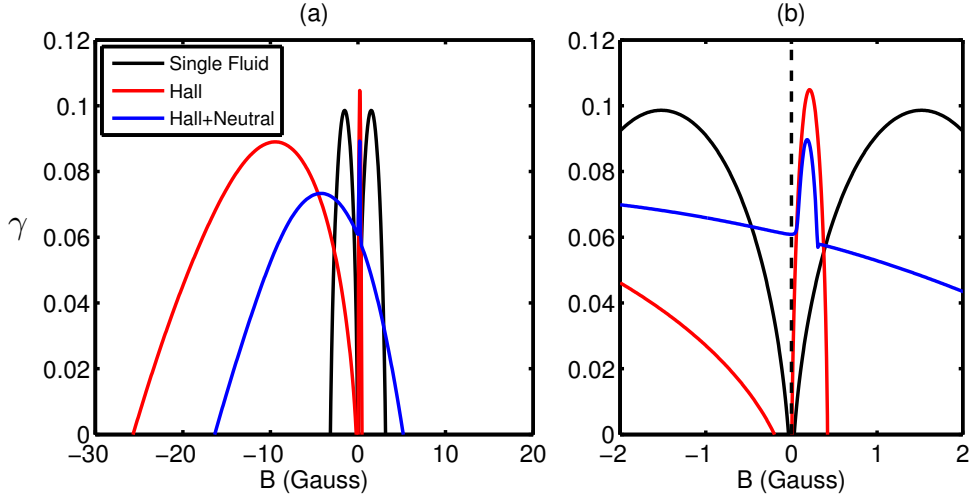


FIGURE 5. Growth rate, γ in units of Ω_1 , plotted as a function of applied magnetic field. The different curves present the single fluid MHD case, the inclusion of the Hall term and the inclusion of neutral charge exchange collisions. For this plot $n_e = 10^{12} \text{cm}^{-3}$ and $P_0 = 10^{-5}$ torr. (a) The full range of magnetic field that gives positive MRI growth rates. (b) A close-up view near $B_0 = 0$ shows the small (less than earth field) positive B_0 branch for the Hall and Hall+Neutral cases.

in the linearized momentum equation. Equations (3.5)-(3.6) are solved for axisymmetric modes using a standard finite difference method assuming no-slip, non-conducting side walls and periodicity in the axial direction. We do not take into account the multicusp magnetic field, details of the plasma confinement and driving near the walls. For TCF study we assume that the boundary toroidal velocities are given. By assuming axial periodicity we also ignore the presence of top and bottom endcaps, thus neglecting the possibility of the Ekman circulation and Hartmann layers. These assumptions greatly simplify present analysis, allowing us to focus on the global MRI physics and not on the boundary effects.

The neglected boundary effects are clearly of great importance in the MRI experiments (e. g., Gissinger *et al.* (2012)), but they deserve a separate detailed study. In particular, correct boundary conditions near the multicusp edge must be determined by values of viscosity and resistivity in that magnetized region. Empirical measurements and PIC simulations will be needed in order to understand this rather complicated non-MHD boundary condition. In our current model viscosity and resistivity are spatially uniform and calculated for unmagnetized plasma core. Nonetheless, we expect that such approximation still gives us reliable estimates for the parameters required for observing the MRI in PCX.

4. Magnetorotational Instability in Taylor-Couette Flow

Unless otherwise noted, all the analysis in this section is done assuming a singly ionized ($Z = 1$ and $n_e = n_i \equiv n$) helium plasma with $T_e = 12$ eV and $T_i = 0.4$ eV. Fixing the temperatures allows viscosity to vary only with density and resistivity, η , to be mostly fixed (there is a weak density dependence). The dimensions of this system are $r_{inner} = 0.1$ m, $r_{outer} = 0.4$ m, and $H = 0.8$ m, where the height determines the axial wave-number $k_z = 2\pi/H$. A modified TCF profile, as defined in Eq. (2.1), is used for this analysis.

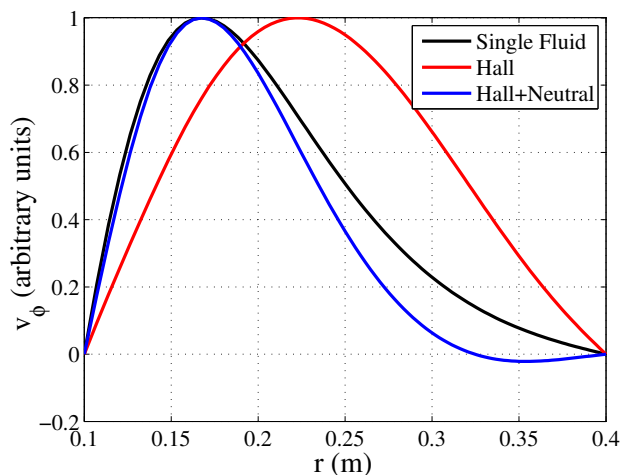


FIGURE 6. Toroidal velocity profiles of the most unstable eigen-modes in the Taylor-Couette flow. Corresponding normalized growth rates are $\gamma = 0.087$ for single fluid MHD, $\gamma = 0.043$ for Hall MHD, $\gamma = 0.063$ for Hall MHD with neutrals. Plasma parameters are the same as in Fig. 5. The magnetic field is $B_0 = -2$ gauss.

The boundary flow velocities are chosen to give a $v_\phi \propto 1/r$ profile when no neutrals are present. A $v_\phi \propto 1/r$ profile is marginally Rayleigh stable (but fully stable when viscosity is included) and meets the ideal-MRI condition. For this analysis an inner velocity of $v_{inner} = 10$ km/s was chosen, which sets $v_{outer} = 2.5$ km/s when a $v_\phi \propto 1/r$ profile is desired. All of these fixed values fall into the range of expected parameters and flows for PCX-U.

4.1. Linear Stability Analysis

Figure 5 highlights the effects of the Hall and neutral collision terms on MRI in TCF. This plot was produced at a density of $n = 10^{12}$ cm $^{-3}$ and a neutral pressure of $P_0 = 10^{-5}$ torr ($n_0 \sim 3.2 \times 10^{11}$ cm $^{-3}$ for room temperature neutrals). For the single fluid case, both the Hall and neutral collision effects are removed leaving growth rates that are insensitive to the direction of B_0 . When the Hall term is included, positive growth rates are found for a large range of B_0 antiparallel to axis of rotation, which corresponds to negative values of B_0 in this analysis. Finally, if the neutral collision term is included the growth rate is slightly reduced and the magnetic field at the peak growth rate is smaller in magnitude. Increased shear in the modified velocity profile causes a hydrodynamic instability (positive growth rate at $B_0 = 0$) at this particular plasma density and neutral pressure. The examples of the eigen-modes for these three cases are given in Fig. 6.

When the dimensionless parameter $\mu \equiv L/L_\nu$ gets large the neutral-drag modified TCF profile becomes hydrodynamically unstable. Under this condition the momentum injected at the inner and outer boundaries does not couple across the whole profile. This leads to increased shear at the outer boundaries of the flow. If the shear is great enough, $\partial(r^2\Omega)/\partial r$ reaches a negative value near the inner boundary, causing the hydrodynamic instability (instability at $B_0 = 0$). This analysis attempts to find a region in parameter space where this hydrodynamic instability is not present (μ is sufficiently small) and the MRI can still be excited with a weak B_0 .

By fixing, T_e , T_i , V_1 , V_2 and the dimensions of the system, the remaining variable plasma parameters are the plasma density, n ; the neutral pressure, P_0 ; and the magnetic

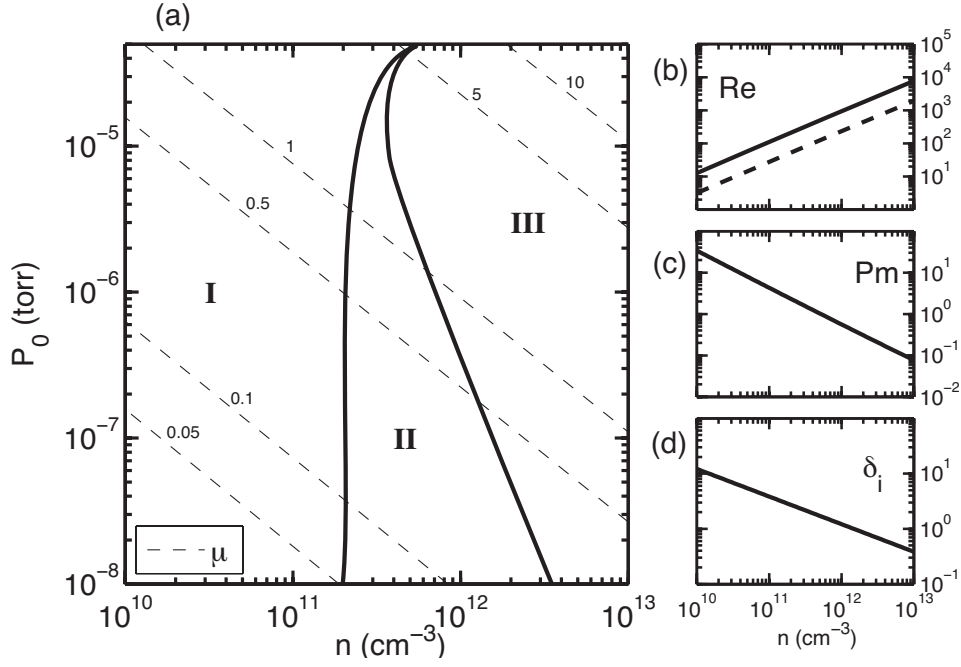


FIGURE 7. (a) Stability curves as functions of n and P_0 . For each n and P_0 the maximum growth rate in the range $B = -300$ to 100 Gauss is used to determine stability. Region I is stable. Region II is hydrodynamically stable, but unstable to the MRI. Region III is hydrodynamically and MRI unstable. Contours of μ are also plotted. On the right, the density dependence of (b) Re for both V_1 (solid) and V_2 (dashed), (c) $Pm \equiv Rm/Re$, and (d) δ_i are plotted to highlight how relevant dimensionless parameters scale with density.

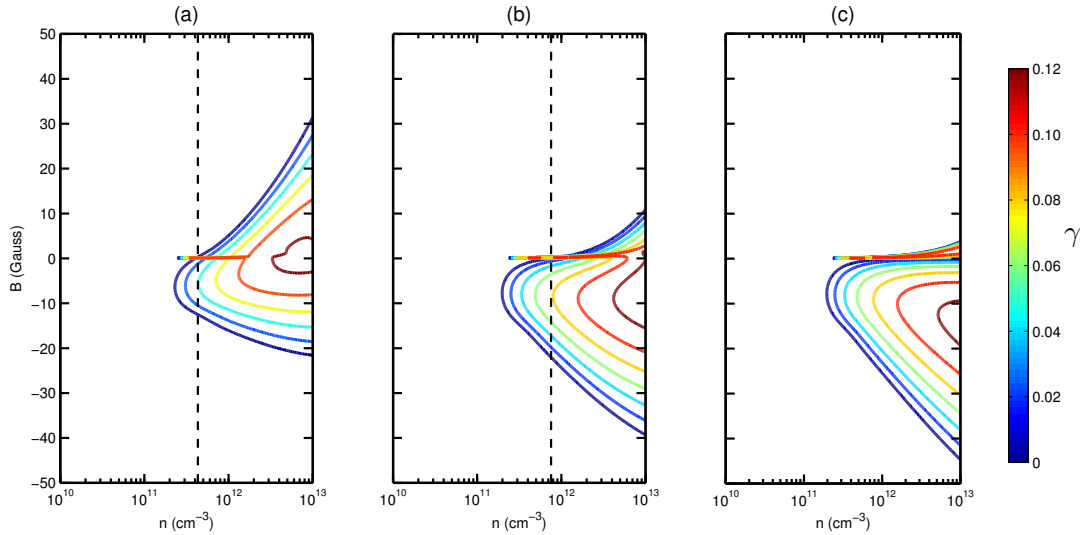


FIGURE 8. Contours of normalized growth rate γ as a function of density and applied magnetic field for the case with (a) $P_0 = 10^{-5}$ torr, (b) $P_0 = 10^{-6}$ torr and (c) no neutrals. The dashed vertical line represents the density at these neutral pressures above which the flow becomes hydrodynamically unstable.

field B_0 . Such a scan provides a range over which plasma physics phenomena can affect the onset of the MRI. Given these three variables, the dimensionless parameters of interest to this analysis have the following dependencies:

$$\delta_i \propto n^{-1/2} \quad (4.1)$$

$$\mu \propto (nP_0 \ln \Lambda_{ii})^{1/2} \quad (4.2)$$

$$M_A \propto n^{1/2} B_0^{-1} \quad (4.3)$$

$$Re \propto n \log \Lambda_{ii} \quad (4.4)$$

$$Pm \propto (n \log \Lambda_{ii} \log \Lambda_{ei})^{-1} \quad (4.5)$$

where $\log \Lambda_{ii}$ and $\log \Lambda_{ei}$ are the weakly density dependent Coulomb logarithms for ion-ion and electron-ion collisions, respectively.

Figure 7 shows instability regions as functions of n and P_0 . Region II represents the region where a MRI experiment would need to operate. Here flowing plasmas are hydrodynamically stable, but an applied axial magnetic field sets off the MRI. It is clear that to ensure that an experiment is in region II with these fixed temperatures and flow velocities, the neutral pressure must be as low as possible and the density must be $n \sim 0.2 - 2 \times 10^{12} \text{ cm}^{-3}$. At higher neutral pressures and higher densities, μ can become of order unity, at which point the shear in the velocity profile caused by neutral drag is large enough to trigger hydrodynamic instabilities (region III). The MRI threshold appears to be set mainly by the density. For densities less than approximately $2 \times 10^{11} \text{ cm}^{-3}$, the viscosity is large enough to damp out the MRI. PCX currently operates in region I. By boosting confinement (increasing the volume to loss-area ratio), PCX-U is expected to fall inside Region II.

For fixed neutral pressures, Fig. 8 shows the effect of the Hall term on the MRI stability. At lower densities where the Hall effect plays the largest role, positive MRI growth rates occur for negative values of B_0 . This corresponds to the requirement that the flow be antiparallel to the magnetic field. As the density increases and the Hall effect weakens some positive growth rates appear for positive values of B_0 . When neutral collisions are included, the asymmetry from the Hall effect is present up to large densities where the flow becomes hydrodynamically unstable. The small positive B_0 branch also persists throughout the density scan (spike-like structures in Fig. 8), but positive growth rates in this branch only occur for very small values of B_0 (less earth field).

4.2. Nonlinear Dynamics

This subsection presents the results of nonlinear dynamics of the axisymmetric MRI in TCF. Fixing the magnetic field at $B = -2$ gauss, density at $n_e = 10^{12} \text{ cm}^{-3}$ and assuming no neutrals, the full nonlinear system (3.1)-(3.4) is evolved in time for single-fluid and Hall MHD cases. Fig. 9 shows the kinetic and magnetic energy time-dynamics for these two respective cases. The interesting points here are that the saturated state in Hall MHD has only even axial harmonics ($k_z = 0, 4\pi/H, 8\pi/H, \dots$) and the saturation level of magnetic energy for non-zero k_z is much lower than in the MHD case. Fig. 10 shows the structure of velocity and magnetic field in the saturated phase of MRI for single-fluid MHD and Hall MHD cases. The saturated magnetic field in Hall MHD is not much different from the originally applied vertical field, as should be expected from consideration of energy evolution plots. However, in the Hall MHD saturated state strong (up to 2 km/s) equatorial jets are produced. Using either mach probes or the Fabry-Perot system (which is theoretically capable of ~ 10 m/s velocity resolution), these strong radial jets will be easily diagnosed, providing evidence of the MRI in PCX-U.

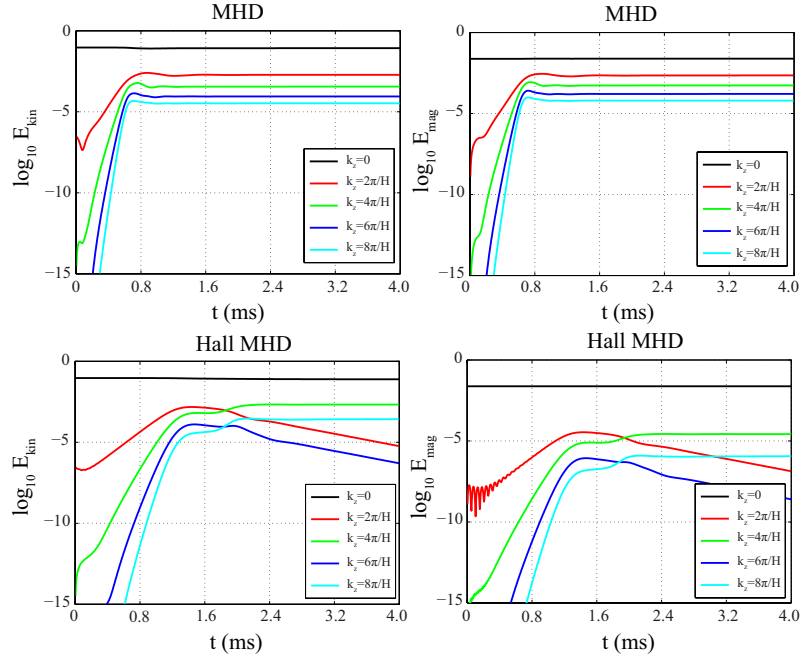


FIGURE 9. Time evolution of the magnetic and kinetic energies for both the single fluid and Hall-MHD cases.

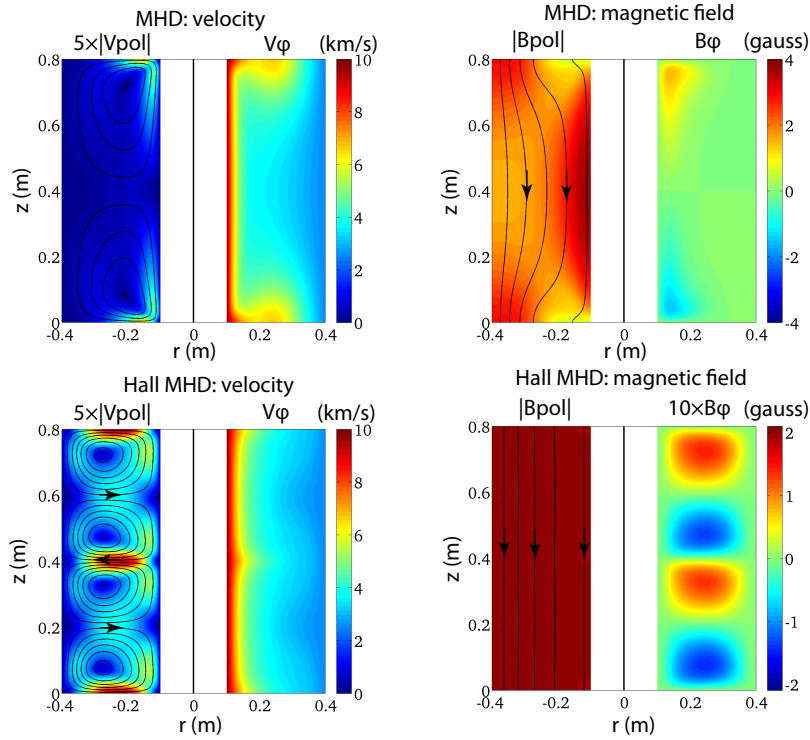


FIGURE 10. Saturated structure of the velocity and magnetic fields for $n_e = 10^{12} \text{ cm}^{-3}$ with no neutrals in both the single fluid and Hall-MHD cases. The applied field is $B_0 = -2$ Gauss.

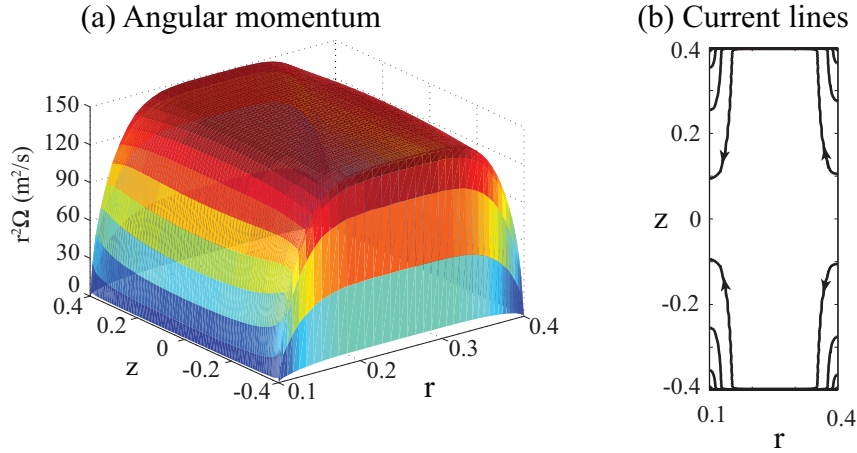


FIGURE 11. Equilibrium electrically driven flow in single fluid MHD: (a) angular momentum profile, (b) current lines in $r - z$ plane. Narrow Hartmann layers are visible near the top and bottom endcaps. Calculations are done for a helium plasma with density $n = 10^{12} \text{ cm}^{-3}$, electron temperature $T_e = 12 \text{ eV}$, ion temperature $T_i = 0.4 \text{ eV}$, total radial current $I_0 = 100 \text{ A}$ and axial magnetic field $B_0 = 10 \text{ Gs}$ (corresponding to $Re = 18$, $Rm = 10$, $Ha = 385$).

5. Electrically Driven Flow

In addition to reaching relevant parameter regimes, achieving flows capable of exciting the MRI is another task for PCX-U. Reaching high flow speeds on the inner boundary has proven to be difficult due to the space and power constraints of the center column assembly. Electrically driven flow (EDF) offers an alternative to Taylor-Couette flow that does not require inner boundary string electrodes.

In EDF a radial electrical current flowing through uniform axial magnetic field creates $\mathbf{J} \times \mathbf{B}$ torque, which acts as the azimuthal body force. The resulting azimuthal velocity in EDF for the bulk of the fluid has $av_\phi \propto 1/r$ profile. As opposed to TCF, the EDF profile shape is unchanged for different magnitudes of total radial current. This removes the freedom of creating an arbitrary azimuthal velocity profile guaranteeing a $1/r$ profile throughout the bulk volume, which is Rayleigh stable when viscosity is included and meets the ideal-MRI conditions.

In PCX-U, the Helmholtz coil supplies an axial magnetic field while a single cathode or anode can be placed in the center of the vessel and biased to electrodes on the outer wall to draw the cross field current. The simplicity of this system is experimentally very attractive because a center core assembly is not required.

In order to increase the current output of PCX cathodes lanthanum hexaboride (LaB6) will be used instead of thoriated tungsten for EDF. This material has an extremely low work function and when heated is a superb electron emitter. LaB6 cathodes used in MPDX can typically draw tens of amperes of current, which represents an order of magnitude increase over the tungsten PCX cathodes (Cooper *et al.* 2014).

5.1. Equilibrium

Analysis of EDF in relation to the MRI has been presented in various parameter regimes using dissipative single-fluid MHD (Noguchi & Pariev 2003; Khalzov *et al.* 2006, 2010). In this analysis Hall and neutral collision terms are included to reflect the regime of weakly-ionized sparse plasmas. As an initial step, the axisymmetric equilibrium state ($\partial/\partial t \rightarrow 0$) described by the system of equations (3.1-3.4) is found assuming perfectly

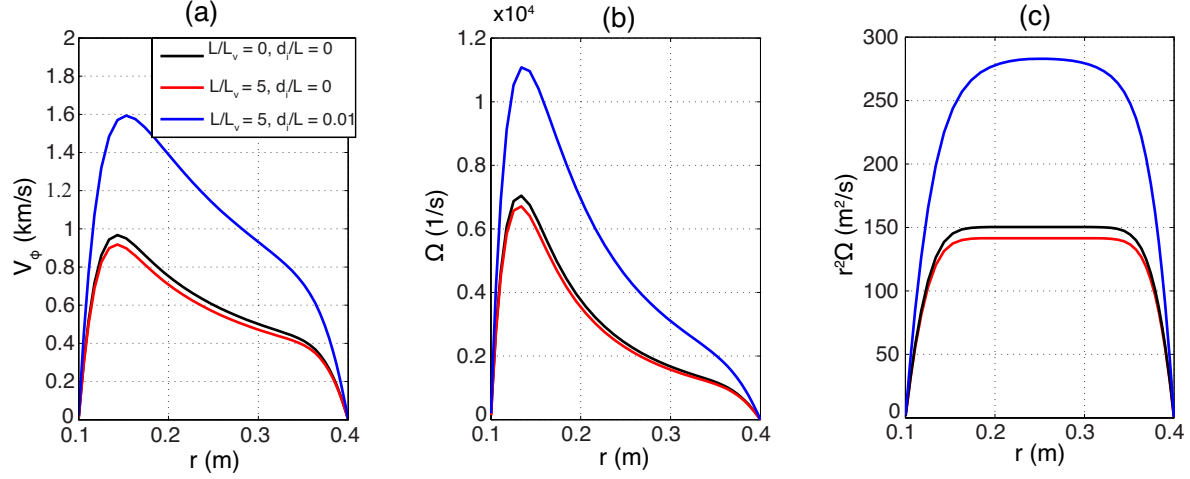


FIGURE 12. The radial profiles of (a) azimuthal velocity, (b) angular frequency, and (c) angular momentum of electrically driven flow showing the effects of neutral drag and the Hall term. Parameters are the same as in Fig. 11.

conducting inner and outer cylinders, insulating top and bottom ends, and no-slip boundary conditions for velocity at the walls. The system is discretized in the two-dimensional r - z domain and solved by an iterative method outlined in (Khalzov *et al.* 2010).

Several key features are present in the equilibrium EDF profiles as shown in Fig. 11. First, there are thin Hartmann layers near the top and bottom ends, which scale like $1/Ha$, and parallel layers near side walls, which scale like $1/Ha^{1/2}$ (Khalzov *et al.* 2010). With the exception of these boundary layers (which are narrow if $Ha \gg 1$), the bulk of the plasma rotates with azimuthal velocity $v_\phi \propto 1/r$ and is practically current-free.

Second, since the driving $\mathbf{J} \times \mathbf{B}$ force for EDF is a body force applied across the whole profile, the neutral drag acts only to uniformly lower the magnitude of the profile. Increased neutral density no longer results in a qualitative change to the shape of the profile like it does for TCF. This simplifies the effects of ion-neutral collisions in the following stability analysis. Similarly, the Hall term acts to uniformly increase the magnitude of the profile (at fixed total radial current). This is illustrated in Fig. 12.

Third, as shown in (Khalzov *et al.* 2010), the magnitude of induced magnetic field scales as Rm/Ha , while the magnitude of poloidal flow scales as Re/Ha^2 . At large Hartmann numbers these quantities become small, therefore they can be neglected in the stability analysis. For the stability analysis, the presence of the boundary layers is also neglected, as they were for the TCF analysis. Additionally it is assumed that the plasma rotates in the uniform axial field B_0 with azimuthal velocity $V_\phi(r) = b/r$, where amplitude b is determined from the equilibrium solver (it depends on total current I_0 , neutral drag and Hall effect).

Note that the neglected boundary layers may lead to some additional parasitic instabilities, especially the layer near the outer wall where the angular momentum is decreasing (and therefore hydrodynamically unstable). This problem can be overcome experimentally by adjusting the positions of the near-wall electrodes so that in addition to bulk forcing, they produce a local drive in the cusp region (like in the TCF) and equalize the boundary and bulk angular momenta.

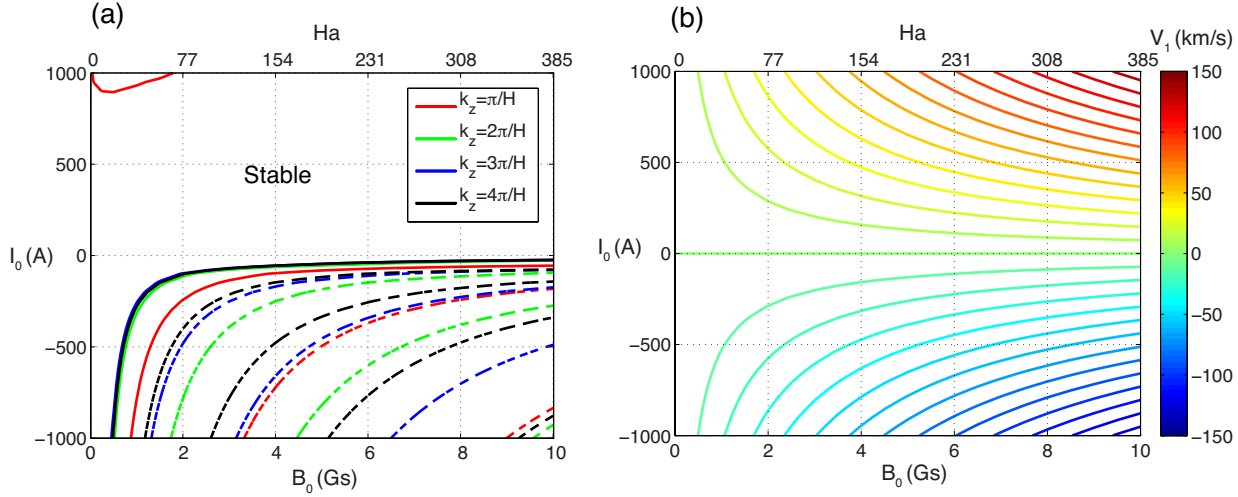


FIGURE 13. (a) MRI regions in electrically driven flow for modes with different axial wave-numbers k_z . Dashed lines of the same color denote stability boundaries for modes with the same k_z but different radial mode numbers. (b) Azimuthal velocity at the inner wall. Plasma parameters are listed in the text. Negative sign of I_0 corresponds to current flowing from the inner to outer wall.

5.2. Stability

The following results are obtained for singly ionized helium plasma with density $n = 10^{12} \text{ cm}^{-3}$, electron temperature $T_e = 12 \text{ eV}$, ion temperature $T_i = 0.4 \text{ eV}$, and neutral pressure $P_0 = 10^{-5} \text{ torr}$ in a cylindrical volume with dimensions $R_1 = 0.1 \text{ m}$, $R_2 = 0.4 \text{ m}$, $H = 0.8 \text{ m}$.

The stability of the equilibrium flow with $V_\phi(r) = b/r$ in an uniform axial field B_0 is studied by solving the eigenvalue problem resulting from the linearized system (3.5-3.6). The MRI boundary as a function of external field B_0 and total current I_0 is given in Fig. 13. The familiar Hall effect is also present in the electrically driven flow where the axis of the flow must be antiparallel to the axial magnetic field to get positive MRI growth rates. This means that current must flow from the inner to outer boundary of the plasma. Experimentally, this means that cathodes at the outer edge must be negatively biased with respect to an anode close to ground placed in the center.

Fig. 13 also demonstrates that several modes with different k_z will be excited almost simultaneously when the MRI threshold is reached. Such a multi-mode instability may lead to a fast development of turbulence, which is another intriguing objective for the proposed plasma MRI experiment.

6. Summary

The prospects for observing the MRI in PCX are good. In this paper, the effects of plasma dynamics pertinent to the PCX regime on the MRI have been studied via a global stability analysis. From this study, an experimentally achievable regime has been found where the MRI should be excited in a laboratory plasma. Experimental considerations have led to an upgrade to put PCX in this regime that is currently underway. Finally, so-called electrically driven flow (EDF) is considered as an alternative to Taylor-Couette flow and is shown to lead to the MRI with PCX-U parameters.

A global stability analysis for weakly-ionized sparse plasmas has highlighted the com-

bined effects of ion-neutral collisions and the Hall term on the MRI. As previously noted, the Hall term leads to a requirement that the seed magnetic field be antiparallel to the axis of rotation for positive MRI growth rates. Ion-neutral collisions effectively add a drag force to the momentum equation. This drag quantitatively changes the Taylor-Couette profile shape and leads to a small region in parameter space where flows are unstable to the MRI while maintaining hydrodynamic stability.

Finally, an experimental configuration for EDF provides an alternative to Taylor-Couette flow that is both experimentally attractive due to its simplicity and less susceptible to large adverse effects due to ion-neutral collisions. EDF can be easily realized in PCX-U with high power LaB6 cathodes capable of driving high Rm flows. Additionally because EDF is driven by a body force, the ion-neutral drag causes no qualitative changes in the $V_\phi(r) \propto r^{-1}$ profile shape. Preliminary global stability analysis of EDF profiles shows that the MRI and possibly MRI turbulence can be excited at experimentally achievable parameters.

This work was funded in part by the National Science Foundation (NSF) and the Center for Magnetic Self Organization in Laboratory and Astrophysical Plasmas (CMSO).

REFERENCES

- BALBUS, S. & HAWLEY, J. 1991 A powerful local shear instability in weakly magnetized disks. *ApJ* **376**, 214–222.
- BALBUS, S. & HAWLEY, J. 1998 Instability, turbulence, and enhanced transport in accretion disks. *Rev. Mod. Phys.* **70**, 1–53.
- BALBUS, S. A. & TERQUEM, C. 2001 Linear analysis of the hall effect in protostellar disks. *Ap. J.* **552**, 235–247.
- CHANDRASEKHAR, S. 1960 The stability of non-dissipative couette flow in hydromagnetics. *Proc. Natl. Acad. Sci.* **46**, 253–257.
- COLLINS, C., CLARK, M., COOPER, C. M., FLANAGAN, K., KHALZOV, I. V., NORNBURG, M. D., SEIDLITZ, B., WALLACE, J. & FOREST, C. B. 2014 Taylor-couette flow of unmagnetized plasma. *Phys. Plasmas* **21** (042117).
- COLLINS, C., KATZ, N., WALLACE, J., JARA-ALMONTE, J., REESE, I., ZWEIBEL, E. & FOREST, C.B. 2012 Stirring unmagnetized plasma. *Phys. Rev. Lett.* **108** (115001).
- COOPER, C. M., WALLACE, J., BROOKHART, M., CLARK, M., COLLINS, C., DING, W. X., FLANAGAN, K., KHALZOV, I., LI, Y., MILHONE, J., NORNBURG, M., NONN, P., WEISBERG, D., WHYTE, D. G., ZWEIBEL, E. & FOREST, C. B. 2014 The madison plasma dynamo experiment: A facility for studying laboratory plasma astrophysics. *Phys. Plasmas* **21** (013505).
- EBRAHIMI, F., LEFEBVRE, B., FOREST, C.B. & BHATTACHARJEE, A. 2011 Global hall-mhd simulations of magnetorotational instability in a plasma couette flow experiment. *Phys. Plasmas* **18** (062904).
- GISSINGER, C., J., GOODMAN & JI, H. 2012 The role of boundaries in the magnetorotational instability. *Phys. Fluids* **24** (074109).
- HERSHKOWITZ, N., LEUNG, K. N. & ROMESSER, T. 1975 Plasma leakage through a low- β line cusp. *Phys. Rev. Lett.* **35** (277).
- KATZ, N., COLLINS, C., WALLACE, J., CLARK, M., WEISBERG, D., JARA-ALMONTE, J., REESE, I., WHAL, C. & FOREST, C.B. 2012 Magnetic bucket for rotating unmagnetized plasma. *Rev. Sci. Instr.* **83** (063502).
- KHALZOV, I. V., ILGISONIS, V. I., SMOLYAKOV, A. I. & VELIKHOV, E. P. 2006 Magnetorotational instability in electrically driven flow of liquid metal: Spectral analysis of global modes. *Phys. Fluids* **18** (12).
- KHALZOV, I. V., SMOLYAKOV, A. I. & ILGISONIS, V. I. 2010 Equilibrium magnetohydrodynamic flows of liquid metals in magnetorotational instability experiments. *J. Fluid Mech.* **644**, 257–280.

- KUNZ, M. & LESUR, G. 2013 Magnetic self-organization in hall-dominated magnetorotational turbulence. *MNRAS* **434** (2295).
- LESUR, G., KUNZ, M. & FROMANG, S. 2014 Thanatology in protoplanetary discs. *A&A* **566** (A56).
- LONGARETTI, P. Y. & LESUR, G. 2010 Mri-driven turbulent transport: the role of dissipation, channel modes and their parasites. *A&A* **516** (A51).
- NOGUCHI, KOICHI & PARIEV, VLADIMIR I. 2003 Magnetorotational instability in a couette flow of plasma. *AIP Conference Proceedings* **692** (1), 285–292.
- VELIKHOV, E. P. 1959 Stability of an ideally conducting liquid flowing between cylinders rotating in a magnetic field. *J. Exptl. Theoret. Phys.* **36**, 1398–1404.
- WARDLE, M. 1999 The balbus-hawley instability in weakly ionized disks. *Mon. Not. R. Astron. Soc.* **307**, 849–856.